



Effects of Airfoil Parameters on Aerodynamic Characteristics Under 3,000,000 Reynolds Number and 4° Angle of Attack Conditions

Chennuo Zeng

Faculty of Science and Engineering, University Nottingham Ningbo China, Ningbo, 315100, China

ssycz7@nottingham.edu.cn

Abstract. The aerodynamic performance of airfoils for fluid analysis has essential applications in aerospace applications and renewable energy. The wind tunnel is a kind of mature analysis method. However, for non-professional organisations or individuals, the financial demands of building a full-size wind tunnel to carry out start-up analyses of an airfoil would be unacceptable. In addition to size constraints, the difficulty of maintenance and power consumption are also disadvantages of wind tunnel experiments. In this research, the aerodynamic performance of the airfoil is analyzed using computational fluid dynamics (CFD) to reduce the difficulty of fluid simulation. Therefore, the result of the effect from max camber, max camber position and thickness could be measured and calculated. The direction of optimization of the airfoil can be summarized by the analysis of these effects. The lift coefficient can be increased by reducing the thickness increasing the camber or moving back to the max camber position. The drag coefficient can be reduced by reducing both thickness and camber or by moving forward to the max camber position. Numerical simulation and fluid analysis can replace some wind tunnel experiments and flight tests, reducing research costs and improving research efficiency.

Keywords: Computational Fluid Dynamics, 2d-Airfoil, Airfoil Parameters, Specific Condition, Airfoil Optimization

1 Introduction

The aerodynamic performance of airfoils for fluid analysis has essential applications in aerospace applications. Optimize the shape and performance of airfoils through fluid analysis to improve aircraft lift and reduce drag, thereby improving fuel efficiency and flight performance. Furthermore, in wind power generation, the airfoil is the core component of the wind turbine blade, and its aerodynamic performance directly affects the utilization efficiency of wind energy. Through fluid analysis, the shape and structure of the airfoil can be optimized to improve the lift-to-drag ratio, thus enhancing the power generation efficiency of the wind turbine. By using

aerodynamic analysis, the drag coefficient of the widely used bell-shaped airfoil was confirmed as the lowest compared with the rest of the airfoils in Pavel's research [1]. In 1977, the experiment from Seetharam et al. showed the results of aerodynamic analysis using a tuft survey and oil flow method. This method of rendering fluid flow using equivalent entities is still used by researchers today [2]. The previous experiment from Chung mentioned that Particle Image Velocimetry (PIV) was used in the wind tunnel test [3]. However, Holger's experiments demonstrated that variations in the intensity of the particle image can greatly affect the presentation of the results of fluid studies by the PIV technique [4]. This further demonstrates the high demand for experimental accuracy in the PIV technique, which is commonly used to present results in wind tunnel tests. One of the drawbacks of physical simulation is that the presentation of experimental results must require mechanical or electronic sensors to convert the measured results into data that can be recognized by computers and mapping software. Errors in solid simulation are unavoidable. Furthermore, large targets must be scaled down in conventional wind tunnel experiments [5]. For researchers and companies, building and maintaining a full-scale model and a larger wind tunnel system will consume more experimental funds.

To deal with the problem, this research used the CFD method to set most of the experiments online. After meshing the 2D airfoil and fluid domain, the solver of the ANSYS Fluent can automatically calculate the results including lift and drag and figure the pressure and velocity cloud diagrams. The error caused by the sensors will be avoided because all these processes are online. The cloud diagrams of pressure and velocity were clear and definite. In this research, CFD was used to calculate the performance of airfoil under specific conditions. Clarify the correct direction of optimization. Compared with the traditional research method, the CFD simulation technology adopted in this paper removes the space limitation and technical threshold brought by the traditional simulation technology.

2 Methodology

2.1 Solver Equations

In this research, the incompressible continuity equation (1) and Navier-Stokes equation (2) are the basic equations of the pressure-based steady solver and $k-\omega$ SST viscosity model.

As shown in Figure 1 from the research from Merryisha and Parvathy, the $k-\omega$ SST model fits the experimental validation well under low-speed conditions [6].

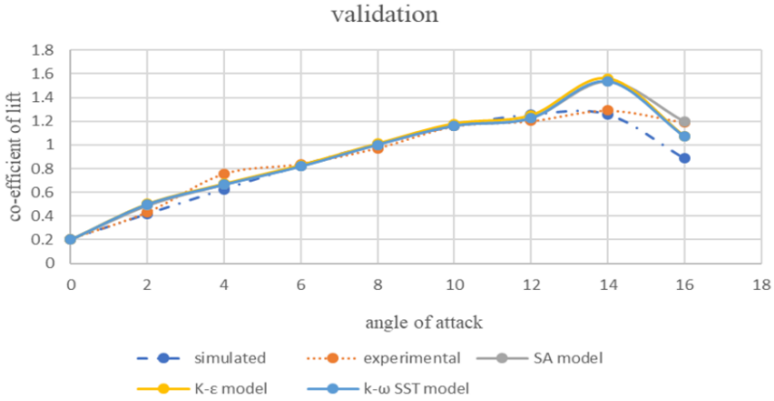


Fig. 1. Validation results of the viscosity models [6]

Incompressible Continuity Equation. In the incompressible continuity equation (1):

$$\frac{\partial \rho}{\partial t} + \frac{\partial \rho u}{\partial x} + \frac{\partial \rho v}{\partial y} + \frac{\partial \rho w}{\partial z} = 0 \tag{1}$$

where $\partial \rho / \partial t$ represents the rate of change of density ρ with time t . This term is usually zero for incompressible fluids because the density does not change with time. For incompressible fluids, this term is usually zero because the density does not change with time.

$\partial \rho u / \partial x, \partial \rho v / \partial y, \partial \rho w / \partial z$ represent the partial derivative of the product of the fluid density in the x, y, z direction and the velocity component u, v, w in the corresponding three directions. This reflects the rate of inflow or outflow of mass in the x -direction.

The physical significance of the entire equation is that the rate of change of mass (i.e., the net mass of inflow and outflow) of the fluid within a control volume is zero, which is consistent with the law of conservation of mass. This indicates that the dispersion of the fluid (i.e., the degree of divergence of the fluid flow) is zero at any given point, further confirming the incompressibility of the fluid.

Navier-Stokes Equation. In the Navier-Stokes equation (2):

$$\rho \frac{\partial V}{\partial t} + \rho(V \cdot \nabla)V = -\nabla p + \rho g + \nabla \cdot \tau \tag{2}$$

Where ρ is the density of the fluid, usually regarded as a constant in incompressible fluids. $\partial V / \partial t$ denotes the rate of change of the fluid velocity vector V with respect to time t , indicating the change of fluid velocity with respect to time. $(V \cdot \nabla)V$ is the convective term representing the effect of the fluid velocity field on the motion of the fluid itself. This term is the dot product of the velocity vector V and the gradient

operator ∇ and reflects the acceleration of the fluid element in the fluid field. $-\nabla p$ is the pressure gradient force, which represents the force due to pressure differences. A negative sign indicates that the direction of the force is opposite to the direction of the pressure gradient. ρg is the gravity term, where g is the gravitational acceleration vector. This term indicates the effect of gravity on the fluid. $\nabla \cdot \tau$ is the viscous stress term, which represents the stress inside the fluid due to viscosity. τ is the stress tensor and $\nabla \cdot$ denotes the scattering operation.

2.2 CST Aerofoil Parameterized

Before airfoil optimization, the airfoil shape is first parameterized. In machine learning generally, the airfoil shape is always represented by a series of points. The advantage of this method is its accuracy. Any software that supports spline can reproduce the airfoil shape accurately. However, the disadvantage is that there are too many parameters. The direct use of the point set as the parameter for optimization is very consuming computational resources and prone to produce non-smooth airfoils or meaningless airfoils resulting in slower convergence and wasted computational resources. The CST parametric method was proposed by Kulfa and Bussollett [7]. It consists of a class function and a shape function, and it can be used to represent the airfoil shape in the same way as the point set. It consists of a class function and a shape function. The class function represents the type of airfoil. The shape function is used to accurately describe the geometry of the airfoil. The specific formula is as follows:

$$Y = C(x) \sum_{r=0}^n a_r S_{r,n}(x) + x \cdot Y_{TE} \quad (3)$$

$$C(x) = k \cdot x^{N_1} (1-x)^{N_2} \quad (4)$$

$$S_{r,n}(x) = k_{r,n} x^r (1-x)^{n-r} \quad (5)$$

where $C(x)$ is the Class function for aerofoil. $N_1 = 0.5, N_2 = 1$ define the rounded wing leading edge and dotted wing trailing edge. $S_{r,n}(x)$ is a partial form function. n is its order and $k_{r,n}$ is the coefficient of the quadratic term associated with the component shape function.

The detailed close-up NACA2412 airfoil is shown in Figure 2.



Fig. 2. Detailed close-up NACA2412 airfoil (Picture credit: Original)

2.3 Fluid Domain Configuration and Segmentation

In this research, NACA2418 and NACA2412 are used as the target aerofoils for the study. The aerodynamic analysis of the aerofoils is carried out by using 15 times chord length C-Type type fluid domain based on the input of the aerofoil's geometrical coordinates and generating the model in the commercial CFD calculation software ANSYS Fluent.

According to the previous research from Sher et al, the C-type fluid domain was tested and was reliable for 2-dimensional airfoil analysis [8]. Besides, the C-type fluid domain could significantly increase the efficiency of variable-angle simulation. The fluid domain configuration is shown in Figure 3.

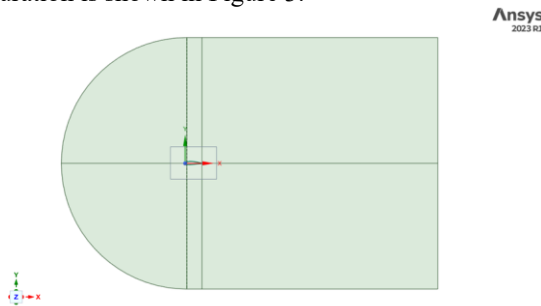


Fig. 3. Fluid domain configuration (Picture credit: Original)

2.4 Meshing

The mesh quality has a direct and significant impact on the simulation results, and a more detailed mesh division has a positive effect on the accuracy of the simulation results quality. Therefore, the C-Type fluid domain used in this paper is divided into six fluid subzones to accurately simulate the analysis results. The mesh cell size of the boundary fluid domain is 0.32m, and the mesh cell size of the near-wing fluid domain

is 6.29×10^{-6} m, which improves the accuracy of the fluid simulation and reduces the computational time and resource consumption through a high bias rate.

The meshing quality comparison between this research and the previous mature research provided by Rao et al is shown in Table 1 [9].

The detailed meshing of this research is shown in Figure 4.

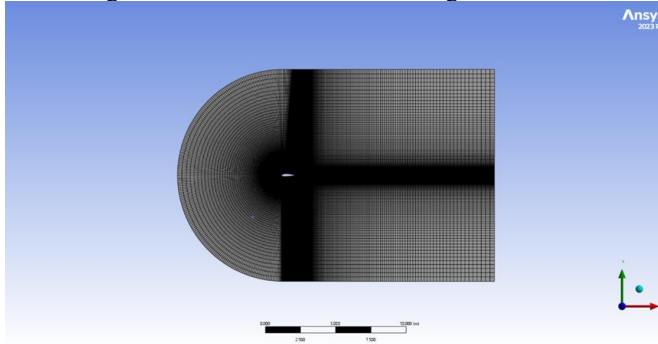


Fig. 4. Detailed Meshing (Picture credit: Original)

Table 1. Meshing Quality Comparison

	This research	The research from Rao et al. [9]
Nodes Number	241,462	82,833
Elements Number	240,500	81,087

2.5 Boundary Conditions and Simulation Settings

Boundary Conditions. The boundary conditions determine the physical shape of the simulation and the control of the variables, ensuring that the simulation can be completed with the preset conditions. The inlet and outlet surfaces are defined to ensure the inlet and outlet positions of the airflow, with the inlet surfaces set as flow control.

In this simulation, Reynolds number (Re) equals 30000, Chord length(C) equals 1m.

At a standard atmospheric pressure, the following parameters are available: Air density (ρ) = 1.225 kg/m^3 , Fluid viscosity (μ) = $1.81 \times 10^{-5} \text{ Pa}\cdot\text{s}$

From Reynolds number equation (6):

$$\text{Re} = \frac{\rho V C}{\mu} \quad (6)$$

The flow speed could be calculated as:

$$V = \frac{\text{Re} \times \mu}{C \times \rho} = \frac{3,000,000 \times 1.81 \times 10^{-5}}{1 \times 1.225} = 44.3 \text{ m/s} \quad (7)$$

The inlet velocity (V) is set to 44.3 m/s and the outlet was set to a gauge pressure of 0 Pa. There was no flow or sticking at the boundary.

Simulation Settings. The simulation setup determines the operational model, the number of iterations, and the residuals needed for the simulation to ensure that the simulation is close enough to the aerodynamic capability under real conditions while ensuring that the arithmetic power is correctly allocated. The operational model is set as a k- ω SST model with 1000 iterations and residuals 1e-6. According to the research from Z. Xu, X. Dong et al., the performance of the k- ω model was reliable, especially in calculating the boundary layer [10]. All simulation settings are shown in Table 2.

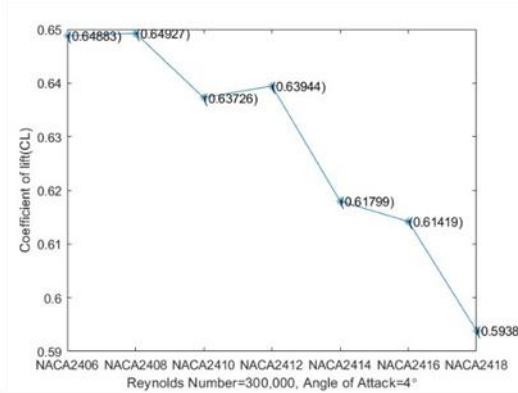
Table 2. Simulation Settings

Solver	Pressure based steady
Viscosity model	k- ω SST
Density(kg/m ³)	1.225
Viscosity(m ² /s)	1.81×10^{-5}
Inlet velocity(m/s)	44.3
Reynolds number	3,000,000
Chord length(m)	1
Momentum	Second Order Upwind

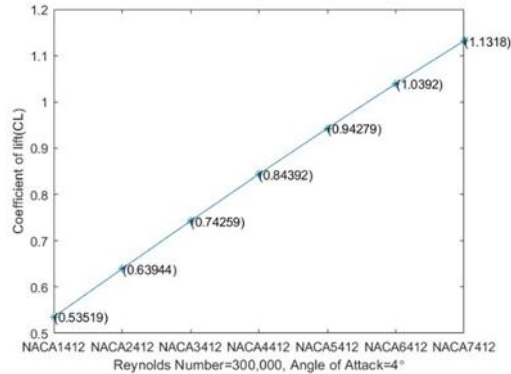
3 Results

3.1 Coefficient of Lift (CL)

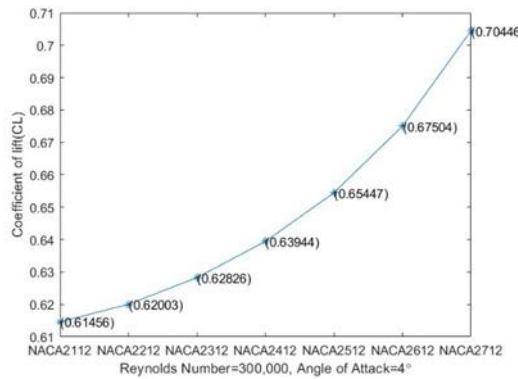
The results of the coefficient of lift about three aerodynamic relative parameters from analysis as shown in Figure 5.



(a)



(b)



(c)

Fig. 5. Coefficient of Lift: (a) Thickness; (b)Max Camber; (c)Max Camber Position (Picture credit: Original)

By analyzing the data in Figure 5, they showed the optimisation trend about improving the lift coefficient in three different aspects.

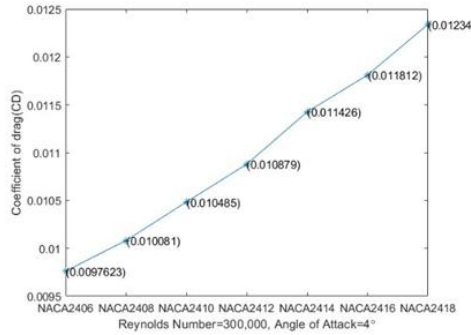
(a) From the Thickness aspect, it demonstrated downward trends with increasing thickness. Even with the rapidly changing figure, the curve still showed a downward trend.

(b) From the Max Camber aspect, the coefficient of lift steadily increased with the increasing of Max Camber.

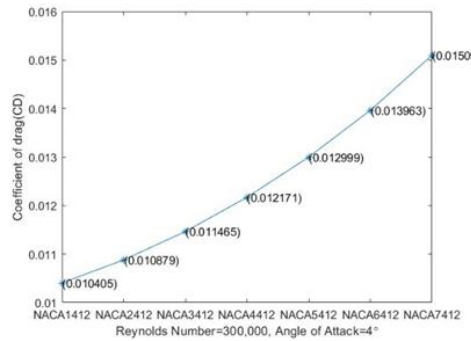
(c) From the Max Camber Position aspect, the growth rate of the lift coefficient increases synchronously with the backward shift of the maximum bending position.

3.2 Coefficient of Drag (CD)

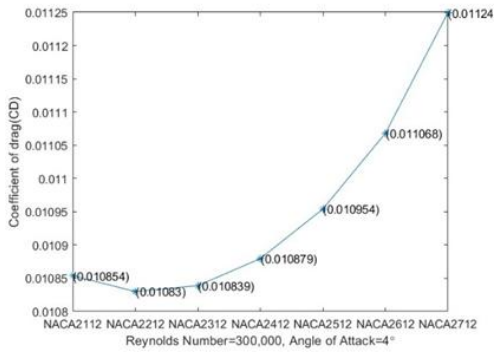
The results of the coefficient of Drag about three aerodynamic relative parameters from analysis are shown in Figure 6.



(a)



(b)



(c)

Fig. 6. Coefficient of drag: (a) Thickness; (b) Max Camber; (c) Max Camber Position (Picture credit: Original)

By analyzing the data in Figure 6, they showed the optimisation trend about improving the drag coefficient in three different aspects.

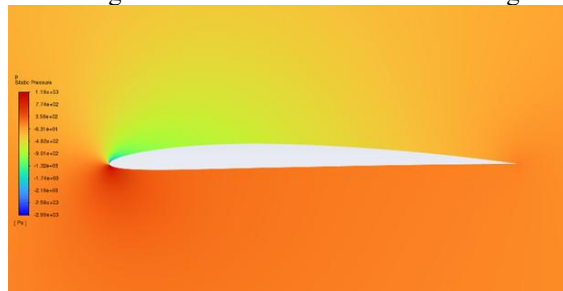
(a) From the Thickness aspect, it showed a steady increase trend with the increasing of the thickness.

(b) From the Max Camber aspect, the growth rate of the coefficient of drag shows a slight tendency to increase with the number of max camber in the overall upward trend.

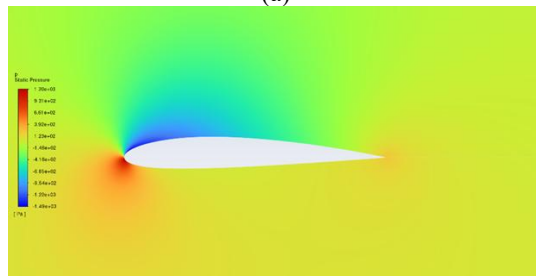
(c) From the Max Camber Position aspect, after a period of decrease from NACA2112 to NACA2212, it still demonstrated rapid growth in subsequent experimental results. That means in the predicted result, the increasing speed of the C_D corresponding to this aspect will increase quickly.

3.3 Pressure

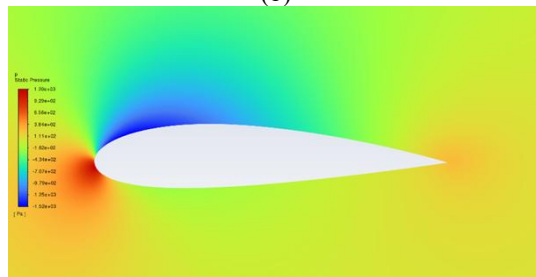
Pressure Changing Based on Thickness. Analysis of the mesh especially those surrounding the airfoil, pressure cloud diagram could be presented on the working window. Pressure cloud diagrams about thickness as shown in Figure 7.



(a)



(b)



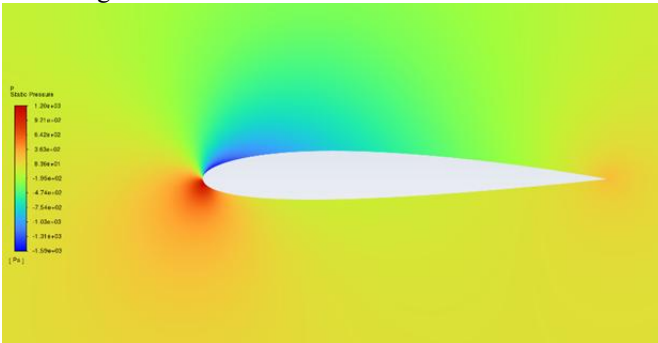
(c)

Fig. 7. Pressure cloud diagram of thickness: (a) Pressure Cloud Diagram (NACA2406); (b) Pressure Cloud Diagram (NACA2412); (c) Pressure Cloud Diagram (NACA2418) (Picture credit: Original)

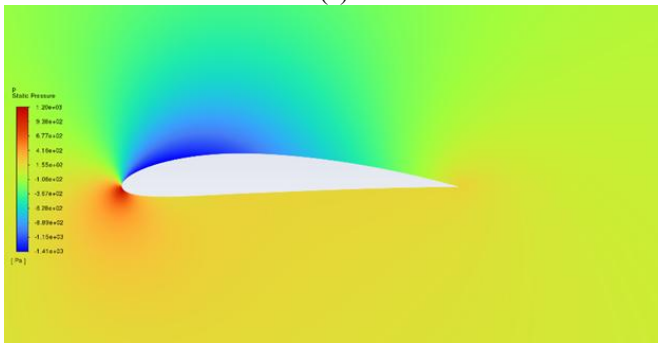
Comparing these three pressure cloud diagrams and the colour bar, the low-pressure area was expanding and the fluid separation was becoming progressively significant with increasing airfoil thickness. The high-pressure centre is concentrated on the leading edge of the wing.

As the thickness of the airfoil increases, the absolute value of the coefficient of pressure (C_p) on the suction surface decreases. This means that the strength of the negative pressure on the suction surface is weakened because the radius of the leading edge of the thicker airfoil is larger and the acceleration of the airflow on the suction surface is not as pronounced as in the case of thin airfoils.

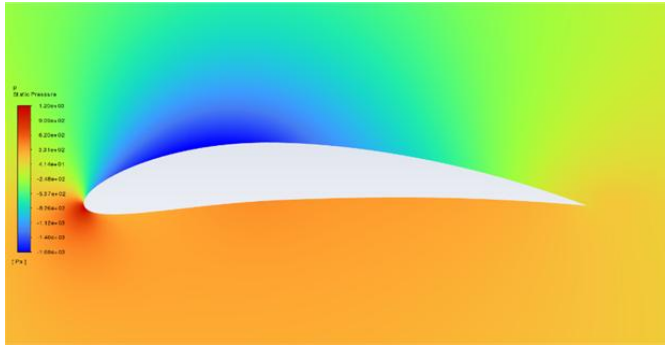
Pressure Changing Based on Max Camber. Pressure cloud diagrams about max camber as shown in Figure 8.



(a)



(b)

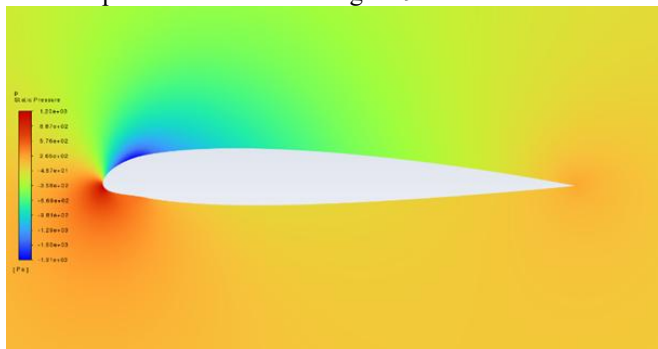


(c)

Fig. 8. Pressure cloud diagram about max camber: (a) Pressure cloud diagram (NACA1412); (b) Pressure cloud diagram (NACA4412); (c) Pressure cloud diagram (NACA7412) (Picture credit: Original)

The pressure difference between the upper surface and lower surface was increasing. The increased camber of the airfoil will make the upper surface more curved. The cross-section of the channel decreases when the fluid flows through the upper surface. The flow velocity accelerates and the pressure decreases according to Bernoulli's principle. The lower surface is relatively flat. The flow velocity changes less and the pressure is relatively high. As a result, the pressure difference between the upper and lower surfaces will increase, resulting in a larger lift force.

Pressure Changing Based on Max Camber Position. The pressure cloud diagrams about the max camber position as shown in Figure 9.



(a)

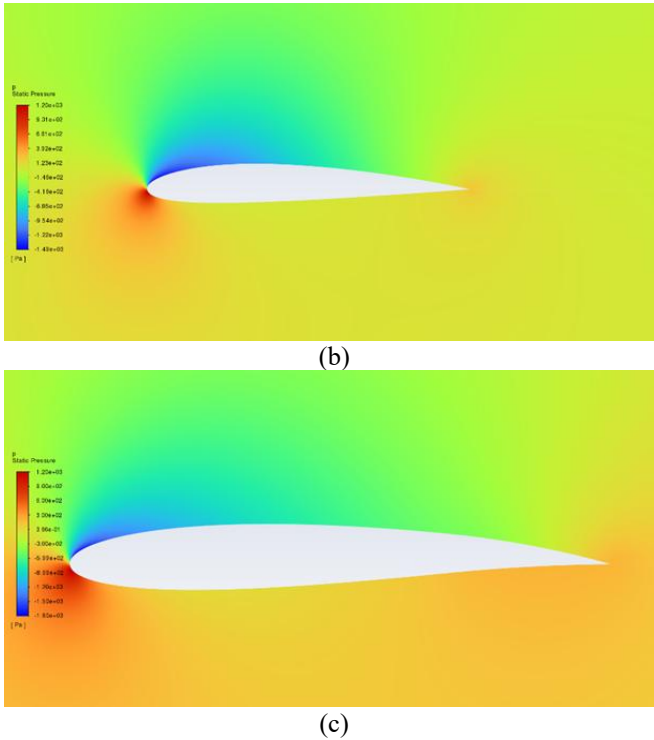


Fig. 9. Pressure cloud diagram about max camber position: (a) Pressure cloud diagram (NACA2112); (b) Pressure cloud diagram (NACA2412); (c) Pressure cloud diagram (NACA2712) (Picture credit: Original)

After the max camber position was shifted backwards because the setback camber allows for a smoother acceleration of the airflow over the upper surface. The negative pressure zone on the upper surface extended backwards and the peak negative pressure appeared to decrease to a certain extent, but the range of the negative pressure zone increased.

3.4 Velocity

Velocity Changing Based on Thickness. Because in this analysis, the airfoils were set as immobile entities. Simulated the aerodynamic behaviour of a wing in a specific condition by controlling the fluid flow rate. The velocity cloud diagram of thickness is shown in Figure 10.

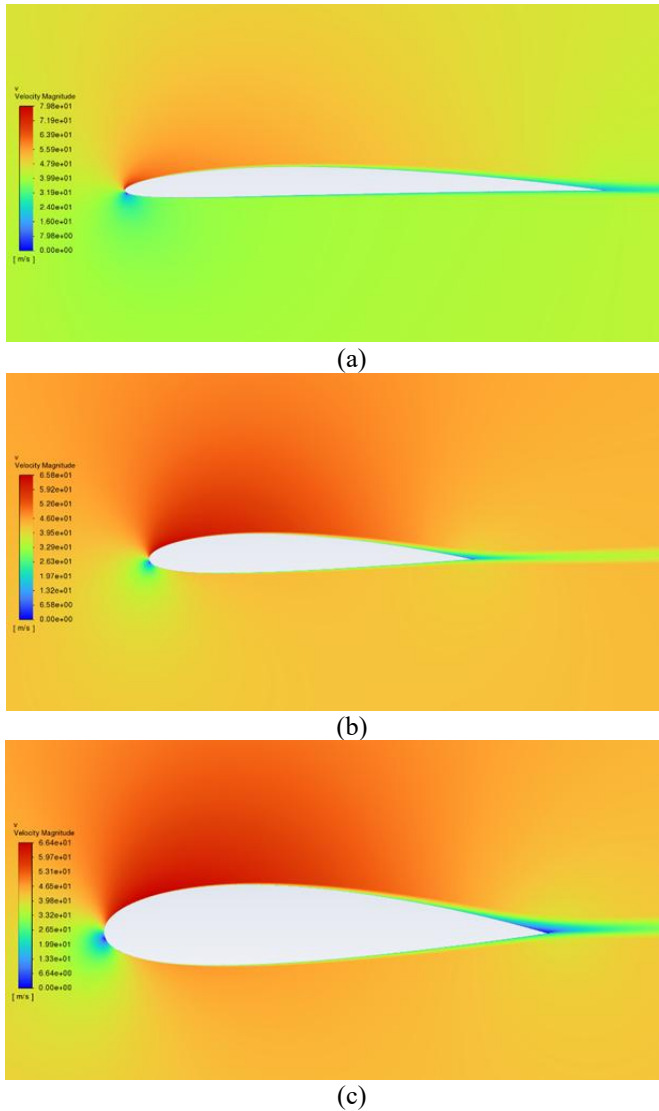


Fig. 10. Velocity cloud diagram about thickness: (a) Velocity cloud diagram (NACA2406); (b) Velocity cloud diagram (NACA2412); (c) Velocity cloud diagram (NACA2418) (Picture credit: Original)

As the thickness of the airfoil increases, the velocity difference between the upper and lower surfaces decreases. An increase in airfoil thickness causes a change in the flow velocity distribution on the upper surface. At small angles of attack, the upper surface of thick airfoils has more balanced flow changes because of its small curvature change.

Velocity Changing Based on Max Camber. The velocity cloud diagram about Max Camber as shown in Figure 11.

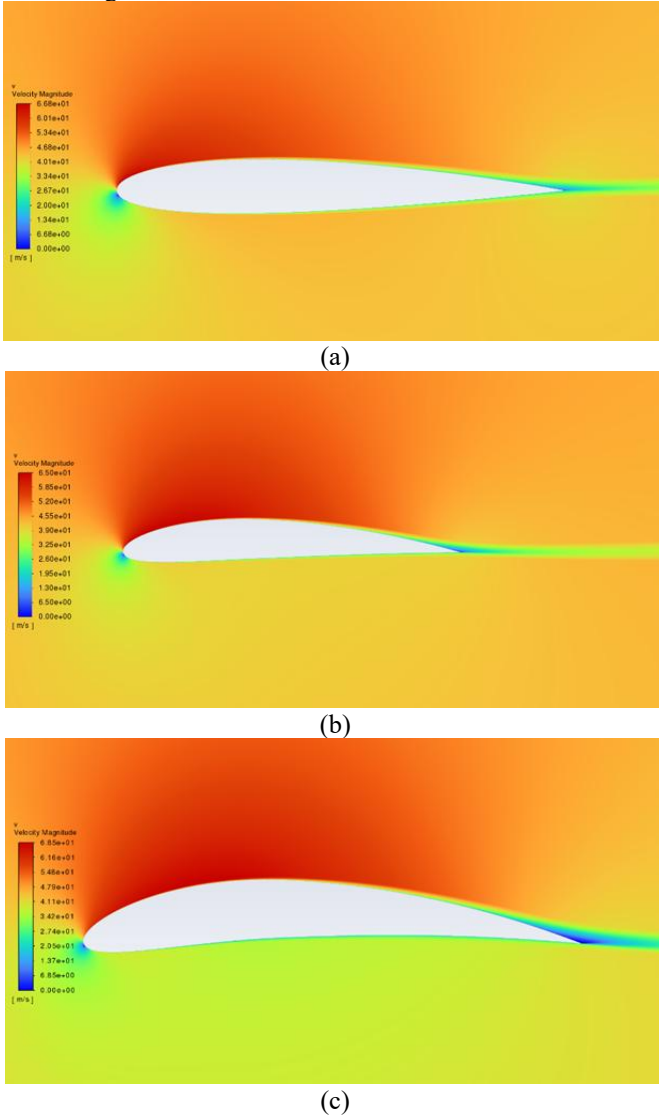


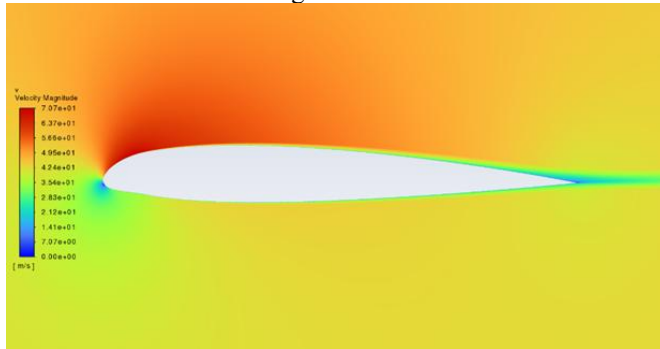
Fig. 11. Velocity cloud diagram about max camber: (a) Velocity cloud diagram (NACA1412); (b) Velocity cloud diagram (NACA4412); (c) Velocity cloud diagram (NACA7412) (Picture credit: Original)

As the maximum camber of the airfoil increases, the curvature of the upper surface becomes more significant and the airflow needs to go through a longer path through the upper surface, while the lower surface is relatively flatter and the airflow path is shorter. According to Bernoulli's equation, the flow velocity is inversely proportional

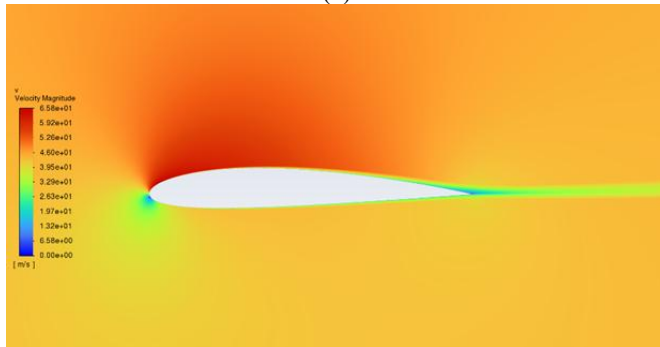
to the pressure, as the flow velocity on the upper surface increases, the flow velocity on the lower surface is relatively low, so the velocity difference between the upper and lower surfaces will increase.

With the increasing air friction mentioned in the max camber-based pressure analysis, the velocity decelerated. Hence, the fluid separation became more conspicuous.

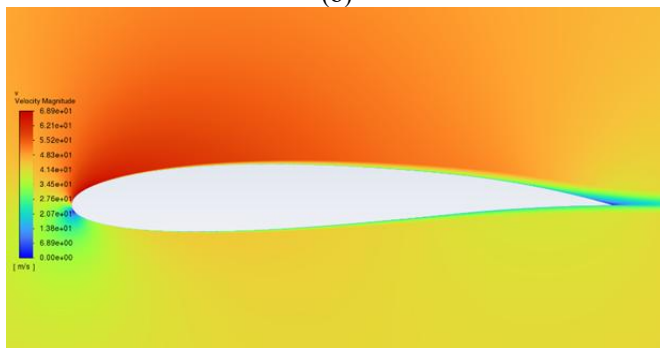
Velocity Changing Based on Max Camber Position. The velocity cloud diagram of the Max Camber Position is shown in Figure 12.



(a)



(b)



(c)

Fig. 12. Velocity cloud diagram about max camber position: (a) Velocity cloud diagram (NACA2112); (b) Velocity cloud diagram (NACA2412); (c) Velocity cloud diagram (NACA2712) (Picture credit: Original)

After the max camber position is shifted back, the range of the negative pressure zone on the upper surface is enlarged, and the peak negative pressure may be reduced, but the overall velocity distribution is more uniform. This change is conducive to improving the aerodynamic performance of the airfoil, especially in low-speed flight conditions.

A rearward shift of the max camber position will result in a lower peak suction at the leading edge and a reduction in the backpressure gradient, thus delaying the stall angle of attack. Meanwhile, the camber position change of the trailing edge affects the separation characteristics of the airflow, and the optimized trailing edge of the airfoil can reduce the separation zone and improve the aerodynamic performance.

4 Conclusion

In the present research, hydrodynamic aerodynamic analyses in CFD are used. The effect of three parameters, airfoil thickness, airfoil max camber and airfoil max camber position on the aerodynamic performance of the airfoil at 4° angle of attack and 300,000 Reynolds number.

In this research, the following conclusions were obtained:

With the increase in thickness, the lift coefficient increases, the drag coefficient decreases, the low-pressure area expands, the fluid separation is significant, the high-pressure centre is concentrated in the leading edge, and the velocity difference between the upper and lower surfaces decreases. With the increase of the maximum camber, the pressure difference and velocity difference between the upper and lower surfaces increase, resulting in a decrease in the lift coefficient. Fluid separation is more obvious, and the drag coefficient is reduced. When the maximum bending position moves backwards, the negative pressure area on the upper surface expands. The decrease of peak negative pressure makes the drag coefficient decrease, but the increase of negative pressure area makes the lift coefficient increase. The overall velocity distribution is more uniform, the back pressure gradient is reduced, and the stalling Angle of attack is delayed.

This study provides a reliable and convenient way to study wing initiation analysis under specific conditions. The direction of improvement is clarified for the optimization of airfoils under specific conditions. However, the airfoil analysis in this research was limited to a 2D simulation. There are more interfering factors to the simulation in the real airfoil analysis. The present $k-\omega$ SST model may not be able to capture the rotationally induced changes in turbulence characteristics with complete accuracy when dealing with rotating flows. With the advancement of analysis techniques and the maturity of computational models, the accuracy and reliability of aerodynamic analyses of airfoils will be further improved.

References

1. Hospodář, P., Drábek, A., Prachař, A: ‘Aerodynamic Design and Strength Analysis of the Wing for the Purpose of Assessing the Influence of the Bell-Shaped Lift Distribution’. *Aerospace*, 2022, 9(1), 13.
2. Seetharam, H., Rodgers, E., Wentz, W.: ‘Experimental studies of flow separation of the NACA 2412 Airfoil at low speeds’.1997 NASA Technical Reports Server (NTRS). <https://ntrs.nasa.gov/citations/19950002355>
3. Jane, L: ‘Particle Image Velocimetry Experiments in a Wind Tunnel to Study Wind-driven Airflow through Building Openings, Indoor Air’ 2014, Hong Kong, (Accessed March 19, 2025), https://tsapps.nist.gov/publication/get_pdf.cfm?pub_id=915632.
4. Nobach, H., Bodenschatz, E: ‘Limitations of accuracy in PIV due to individual variations of particle image intensities’. 2009 *Exp Fluids* 47, 27–38. <https://doi.org/10.1007/s00348-009-0627-4>.
5. Hemsch, Michael J: ‘Global Comparison of CFD and Wind-Tunnel-Derived Force and Moment Databases for the Space Launch System - NASA Technical Reports Server (NTRS).’ 2016 NASA, NASA, ntrs.nasa.gov/citations/20160007695.
6. Samuel, M., Rajendran, P.: ‘CFD Validation of NACA 2412 Airfoil’. 2019. 10.13140/RG.2.2.16245.42723.
7. Brenda K., John B.: ‘"Fundamental" Parametric Geometry Representations for Aircraft Component Shapes,’ 2006. AIAA 2006-6948. 11th AIAA/ISSMO Multidisciplinary Analysis and Optimization Conference.
8. Khan, S., Bashir, M., Baig, M., Mehaboob Ali, F.: ‘Comparing the Effect of Different Turbulence Models on The CFD Predictions of NACA0018 Airfoil Aerodynamics’. 2021. *CFD Letters*, 12(3), 1–10. Retrieved from <https://akademibaru.com/submit/index.php/cfdl/article/view/3219>.
9. Rao, Y., Manohar, M., & Praveen, S.: ‘CFD simulation of NACA airfoils at various angles of attack’. 2021. *IOP Conference Series Materials Science and Engineering*, 1168(1), 012011.
10. Xu, Z., Dong, X., Li, K., Zhou, Q. and Zhao, Y: ‘Study of the Self-starting Performance of a Vertical-axis Wind Turbine’. 2024. *Journal of Applied Fluid Mechanics*, 17(6), 1261-1276.

Open Access This chapter is licensed under the terms of the Creative Commons Attribution-NonCommercial 4.0 International License (<http://creativecommons.org/licenses/by-nc/4.0/>), which permits any noncommercial use, sharing, adaptation, distribution and reproduction in any medium or format, as long as you give appropriate credit to the original author(s) and the source, provide a link to the Creative Commons license and indicate if changes were made.

The images or other third party material in this chapter are included in the chapter's Creative Commons license, unless indicated otherwise in a credit line to the material. If material is not included in the chapter's Creative Commons license and your intended use is not permitted by statutory regulation or exceeds the permitted use, you will need to obtain permission directly from the copyright holder.

